From Metals to Semiconductors: Advancing MXY (M = Ti, Sn, Ir, X = Se, Te, Y = Se, Te) Compounds with Strain Engineering—A Computational Perspective

Munaf Aldaoseri, Zahra Nourbakhsh, and Daryoosh Vashaee**

In this computational study, density functional theory (DFT) is employed to analyze the structural, electronic, elastic, and topological properties of ternary compounds MXY (M = Ti, Sn, Ir, X = Se, Te, Y = Se, Te). The effects of spin–orbit interaction and pressure-induced strain are investigated to understand their influence on the stability, mechanical properties, and electronic behavior, paving the way for potential technological applications. The findings confirm that these compounds are inherently stable in nonmagnetic phases, with spin–orbit interaction critically influencing their energy–volume landscapes. The calculated lattice parameters, ratios of lattice constants, and bulk moduli closely align with existing data, confirming the reliability of our approach. Mechanical assessments reveal distinct behaviors: $IrSe_2$ exhibits the highest stiffness due to pronounced covalent bonding, contrasting with $SnTe_2$'s elastic anisotropy and SnSeTe's nearly isotropic properties. Electronically, most compounds show metallic characteristics, except $SnSe_2$, which behaves as a semiconductor with an indirect, pressure-sensitive energy bandgap. Topological analysis under varying hydrostatic pressures indicates band inversions in $TiSe_2$, $IrSe_2$, and SnSeTe, suggesting topological phase transitions absent in other compounds. This study enriches our understanding of these materials and refines the application of DFT in material design.

1. Introduction

In the interdisciplinary fields of condensed matter physics and materials science, the search for materials with unique electronic and topological properties has intensified, driven by their potential applications in spintronics, quantum information, and quantum computing. Among these, topological materials, including insulators and metals, are particularly notable for their novel quantum states that allow electrons to move along their edges (in 2D systems) or surfaces (in 3D systems) with zero energy loss. This unique characteristic makes them prime candidates for developing advanced topological devices.

The foundational work by Bernevig et al. which introduced a model for understanding topological phase transitions through band ordering, has provided a crucial framework for this research.[1] According to their model, the topological state of a material can be defined by its band order—normal or inverted. Materials with a normal band order are considered topologically trivial, while those with an inverted band order exhibit topologically nontrivial states, a phenomenon often facilitated by the presence of spin–orbit interaction. This interaction is pivotal as it removes the degeneracy of energy bands at symmetry points, leading to band splitting and the potential for band inversion.

Recognizing the importance of external perturbations such as strain in altering the electronic structures of materials, this study focuses on MXY (M = Ti, Sn, Ir; X, Y = Se, Te) compounds. These compounds are chosen for their diverse physical properties and structural versatility, ranging from their use in electronic devices due to their semiconducting properties to potential applications in thermoelectric materials and batteries. Our investigation extends to exploring how spin–orbit coupling and strain engineering influence their structural, electronic, elastic, and topological properties through detailed first-principles calculations based on density functional theory (DFT).

The focus of our computational study is to elucidate the impact of hydrostatic and axial pressures, chemical doping, and impurities on these properties. We employ a detailed analysis of the lattice parameters, bulk modulus, elastic properties, electron density of states, electronic-specific heat, energy bandgaps, and topological phases under varying conditions. This comprehensive

M. Aldaoseri, Z. Nourbakhsh
Faculty of Physics
University of Isfahan
Isfahan, Iran
E-mail: z.nourbakhsh@sci.ui.ac.ir

D. Vashaee
Department of Electrical and Computer Engineering
North Carolina State University
Raleigh 27604, USA
E-mail: dvashae@ncsu.edu

D. Vashaee
Department of Materials Science and Engineering
North Carolina State University
Raleigh 27604, USA

The ORCID identification number(s) for the author(s) of this article can be found under https://doi.org/10.1002/adem.202401492.

DOI: 10.1002/adem.202401492

approach allows us to explore the underlying mechanisms that govern the behavior of these materials under external stresses and their potential for new technological applications.[2–6]

Particularly, we highlight how strain engineering and spin–orbit interactions can significantly alter the electronic and topological behavior of these compounds, a novel aspect of our study that promises to expand the understanding of material properties in significant ways. By documenting how these interactions affect materials such as $TiSe_2$, which exhibits critical phase transitions under specific conditions, our work contributes valuable insights into the design and development of new materials with tailored electronic and topological properties.

Through this paper, we aim to provide a significant contribution to the field by demonstrating the effects of strain and spin–orbit interactions on the material properties of MXY compounds, thereby offering a deeper understanding of their potential applications and behaviors under external perturbations.[7–10]

In the interdisciplinary fields of condensed matter physics and materials science, the quest for topological materials, encompassing topological insulators and metals, has garnered significant attention due to their profound implications for spintronics, quantum information, and quantum computing. These materials, celebrated for enabling the development of cutting-edge topological devices, exhibit a novel quantum state wherein electrons at the edges (in 2D systems) or surfaces (in 3D systems) propagate with zero energy dissipation. This remarkable behavior was rigorously modeled by Bernevig et al. who provided a foundational framework for understanding topological phase transitions through band ordering.[1] Their methodology delineates the topological state of a material based on its band order—normal or inverted. Materials with a normal band order are classified as topologically trivial, whereas those exhibiting an inverted band order, a phenomenon known as band inversion, are deemed topologically nontrivial. This distinction is critically dependent on the spin–orbit interaction, a quantum mechanical phenomenon that lifts the degeneracy of energy bands at symmetry points, resulting in band splitting and, consequently, the potential for band inversion.

The mechanism of topological band inversion, which heralds a phase transition, typically occurs at time-reversal invariant points within the first Brillouin zone, signified by an inversion in the distribution of electrons across the band structure's different parities. This inversion process underscores the utility of band order as a robust method for identifying materials undergoing topological phase transitions while maintaining time-reversal symmetry. Specifically, in 3D materials, the presence of time-reversal symmetry is a prerequisite for band inversion. To facilitate a topological phase transition, it is essential to alter the band order of materials through external perturbations, such as hydrostatic and axial pressures, chemical doping, and the introduction of impurities.[2–6]

The focus of our study extends to MX_2 (M = Ti, Sn, Ir; X = S, Se, Te) transition metal compounds, distinguished by their versatile physical properties. These compounds, with the exception of $IrSe_2$, predominantly feature a van der Waals layered structure in a hexagonal close-packed CdI_2 configuration, referred to as the 1T-structure at room temperature. This configuration entails an octahedral coordination of the metal atom M by six X and Y atoms within the $P\overline{3}m1$ space group.[7–10] In contrast, $IrSe_2$ crystallizes in an orthorhombic structure within the pnma space group.[11–13] The compound $SnSe_2$, known for its small indirect energy bandgap, has piqued the interest of researchers due to its potential electronic device applications.[14–18] This interest is amplified by the covalent bonding between Sn and Se atoms, alongside van der Waals interactions between adjacent layers, marking its semiconductor characteristics. $TiSe_2$, on the other hand, has been spotlighted for its utility as an alternative to graphene in thermoelectric applications and as a cathode material in lithium batteries.[19,20] Predictions by Zhu et al. regarding the topological phase transition of $TiSe_2$ under pressure,[21] alongside investigations into its dynamical properties at varying pressures,[22] reveal critical structural and topological phase transitions at distinct pressure thresholds.

Furthermore, the structural phase transition of $IrTe_2$ has been studied up to 32 GPa using angle-dispersive X-Ray diffraction at room temperature.[23] This research demonstrates that the CdI2-type structure (space group $P\overline{3}m1$) is maintained throughout the entire range of hydrostatic pressure studied. At ≈5 GPa, a monoclinic phase appears, but as the pressure increases, the phase transitions remain incomplete. At 20 GPa, a cubic phase with low density is detected; this density significantly increases following laser heating at this pressure. Ritschel et al.[24] further explored the phase transition of the $IrTe_2$ compound under pressures up to 42 GPa at various temperatures (ranging from room temperature to 420 K) using high-pressure X-Ray diffraction, resulting in a detailed pressure-temperature phase diagram for this compound. Their findings indicate that at zero pressure, the compound is stable in the 1 T-structure ($P\overline{3}m1$) phase without dimers. With increasing pressure, various ordered phases appear and sometimes coexist. At 1.4 GPa, a triclinic lattice symmetry emerges, and at 6.5 GPa, a monoclinic (C_2/c) phase appears, which remains stable up to the highest pressures studied.

The bulk electronic structure of $IrTe_2$ has been studied using angle-resolved photoemission spectroscopy.[25] Investigations into the structural and electronic phase transitions of $IrTe_2$ due to temperature in the presence of strong spin–orbital coupling have been reported,[26–28] indicating a transition from the 1T structure with space group $P\overline{3}m1$ to a monoclinic structure with space group C2/m below 280 K. Studies on the optical properties of $IrTe_2$ compounds using density functional theory band structure for several crystal structures,[29] as well as measurements of polarized Raman scattering of $IrTe_2$ in different stable single crystal structures over the 15–640 K temperature range,[30] have contributed to our understanding. Additionally, the effect of photoelectrons on structural transitions of $IrTe_2$ has been studied using density functional theory,[31] along with reports on the temperature dependence of the conductivity and electrical transport properties of $IrSe_2$.[32,33] The influence of pressure on the various physical properties of MX_2 (M = Ti, Sn, Ir; X = S, Se, Te) compounds has also been extensively studied.[24,34–39]

Building on foundational concepts, our study introduces a novel focus on the dual influences of strain engineering and spin–orbit interaction in shaping the properties of MXY (M = Ti, Sn, Ir; X, Y = Se, Te) compounds. By methodically applying controlled external pressures, we explore and delineate the resultant changes in both the electronic structure and topological phases, offering critical insights into potential applications for next-generation electronic and quantum devices.

Our investigations utilize the hexagonal close-packed CdI_2 configuration in the 1T structure, within the space group $P\bar{3}m1$. This approach ensures that our computational models are robust and accurately representative of real-world material structures.

This research integrates comprehensive analyses of lattice parameters, bulk modulus, elastic properties, electron density of states, electronic-specific heat linear coefficients, energy bandgaps, and topological phases at both zero and varying hydrostatic pressures. Through this rigorous methodology, we aim to significantly enhance the existing body of knowledge on these compounds, facilitating a deeper understanding of their potential technological applications and their responses to external perturbations.

Overall, this study not only illuminates the subtleties of material behavior under strain and spin–orbit interactions but also underscores the significant technological promise of these materials for future applications.

2. Method of Calculations

This study employs density functional theory (DFT) to investigate the physical properties of materials, focusing on the reliable and widely used Kohn–Sham equations for solid-state analyses.[40] We solve these equations via the full potential linear muffin-tin orbital (FP-LMTO) method, utilizing the WIEN2k software package.[41,42] This method separates each unit cell's volume into the interstitial region and nonoverlapping muffin-tin spheres surrounding each atom, each sphere characterized by its radius R_{MT}. Within this framework, basis functions, crystal potential, and charge density are represented by spherical harmonics inside the muffin-tin spheres and plane waves in the interstitial space.

For the treatment of exchange and correlation interactions, we implement the generalized gradient approximation (GGA), using both the Perdew–Burke–Ernzerhof (PBE) method[43] and the Engel–Vosko (GGA-EV) model,[44] as well as the modified Becke and Johnson (mBJ) approach.[45] These approaches are selected for their effectiveness in accounting for the intricate details of exchange and correlation effects, essential for precise property predictions.

The computational setup was meticulously optimized for accuracy, involving the selection of muffin-tin radii ($R_{Ti} = R_{Se} = 2$ a.u. and $R_{Te} = R_{Sn} = R_{Ir} = 2.1$ a.u.), a $16 \times 16 \times 8$ k-point mesh for Brillouin zone sampling, and specific cutoffs for the angular momentum quantum number ($l_{max} = 10$) and plane wave expansion ($K_{max} = \frac{9.5}{R_{MT}}$ (a.u.)$^{-1}$) in the interstitial region. The maximum vector magnitude for Fourier expansions of charge density and potential in the interstitial zone was set at $G_{max} = 15(\text{Ry})^{1/2}$, ensuring the convergence of total energy calculations.

All calculated results, except for those involving the elastic tensor, are performed with an energy convergence threshold of 0.00001 and force reduction on the atoms set to 1 mRy a.u.$^{-1}$. For the elastic tensor calculations, we achieve higher precision by setting the energy convergence to 0.000001 and reducing the force on the atoms to 0.1 mRy a.u.$^{-1}$. This enhanced precision ensures more accurate measurements of the elastic properties, leading to more reliable outcomes in our analysis.

To determine the elastic constants of MXY (M = Ti, Sn, Ir; X = Se, Te; Y = Se, Te) compounds, we utilized the IRELAST package,[46] which employs a second-order derivative framework. Subsequent analyses of these elastic constants were conducted using the ELATOOLS package,[47] facilitating a comprehensive examination of the compounds' mechanical properties.

This methodology, leveraging advanced computational techniques alongside precise parameter selection, lays a solid foundation for our detailed exploration of the MXY compounds, aiming to uncover their structural, electronic, and mechanical attributes.

3. Results and Discussion

3.1. Structural Properties

In our study, we calculated the total energy of MXY (M = Ti, Sn, Ir; X, Y = Se, Te) compounds as a function of volume, examining the effects both with and without relativistic spin–orbit interaction in magnetic and nonmagnetic phases. Specifically, the energy–volume curves for MSeTe (M = Ti, Sn, Ir) in the nonmagnetic phase, as depicted in **Figure 1**, show a significant influence of spin–orbit interaction on their total energy profiles, highlighting its critical role. We also calculated and compared the minimum energy configurations of these compounds in both ferromagnetic and nonmagnetic phases, with results detailed in **Table 1**. These assessments confirm that these compounds are predominantly stable in the nonmagnetic phase.

Additionally, to explore the structural phase transition of the $IrTe_2$ compound under hydrostatic pressure, we computed its total energy for six different crystal structures: orthorhombic (space group Pnma, No. 62), triclinic (space group $P\bar{1}$, No. 2), hexagonal (space group $P\bar{3}m1$, No. 164), monoclinic (space group C2/m, No. 12), cubic (space group $Pa\bar{3}$, No. 205), and tetragonal (space group P42/mnm, No. 136), employing the GGA exchange-correlation potential with spin–orbit interaction. The findings, illustrated in Figure 1, reveal that the hexagonal $P\bar{3}m1$ (No. 164) configuration is the most stable phase for $IrTe_2$.

We also determined the lattice parameters, the ratio of lattice parameters (c/a), and the bulk modulus for these compounds using the GGA exchange-correlation potential, incorporating spin–orbit interaction effects. These computational findings were compared with existing experimental and theoretical data,[9,10,23,34,48–61] as detailed in **Table 2**. The slight variations in the calculated lattice constants, both "a" and "c," compared to other reported values, fall within acceptable limits. These discrepancies can be attributed to inherent differences in theoretical approaches and potential variations in experimental methodologies.

Our calculated values align well with existing theoretical and experimental findings, corroborating the validity of our approach. Notably, the bulk modulus, a measure of a material's resistance to compression, varies across the studied compounds, as presented in Table 2. The analysis suggests that the bulk modulus is influenced by the nature of bonding within the compounds; ionic bonding tends to reduce the bulk modulus due to a decrease in bonding charge, whereas covalent bonding typically enhances it. This correlation is evident in the observed bulk

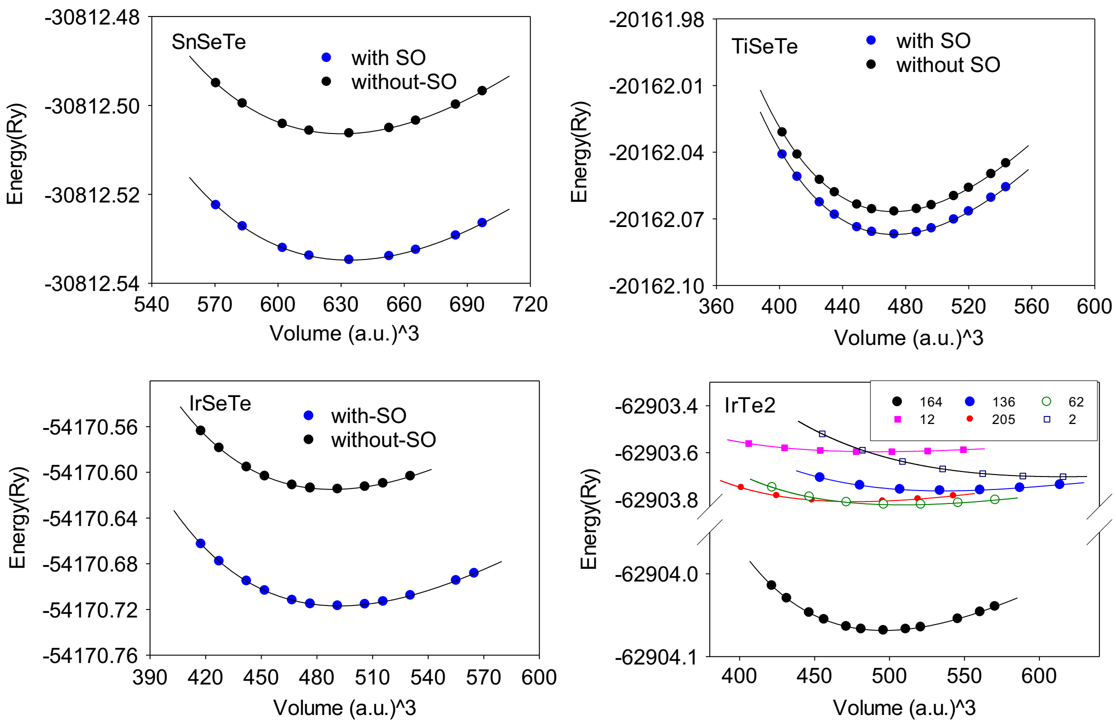

Figure 1. Total energy versus volume for MSeTe (M = Ti, Sn, Ir) compounds within GGA approach in nonmagnetic self-consistent calculations and hexagonal close-packed CdI_2 crystal (space group $P\bar{3}m1$, No. 164), comparing scenarios with and without the relativistic spin–orbit interaction. Additionally, it presents the total energy of the $IrTe_2$ compound as a function of volume within GGA approach in nonmagnetic self-consistent calculations across six different crystal structure types: orthorhombic (space group Pnma, No. 62), triclinic (space group $P\bar{1}$, No. 2), hexagonal (space group $P\bar{3}m1$, No. 164), monoclinic (space group C2/m, No. 12), cubic (space group $Pa\bar{3}$, No. 205), and tetragonal (space group $P4_2/mnm$, No. 136).

Table 1. The calculated equilibrium total energy of MXY (M = Ti, Sn, Ir, X = Se, Te, Y = Se, Te) compounds in magnetic and nonmagnetic in hexagonal close-packed CdI_2 structure within GGA approach with spin–orbit interaction and linear electronic specific heat of these compounds at zero pressure.

Compounds	Equilibrium total energy with spin–orbit interaction (Ry)		γ (mJmol^{-1} K^{-2})
	Ferromagnetic phase	Nonmagnetic phase	
IrSe2	−45437.371	−45437.372	5.09
IrTe2	−62903.817	−62904.068	4.55
IrSeTe	−54170.715	−54170.717	5.59
SnSe2	−22079.217	−22079.218	0
SnTe2	−39545.604	−39545.856	1.42
SnSeTe	−30812.408	−30812.534	2.23
TiSe2	−11428.803	−11428.803	1.93
TiTe2	−28895.171	−28895.439	3.86
TiTeSe	−20162.076	−20162.077	3.47

moduli of IrXY compounds, which are higher than those of TiXY and SnXY compounds. This variation can be attributed to changes in charge density hybridization, which transitions the bonding character from covalent to more ionic as the Ir atom is substituted with Ti and Sn atoms.

To further assess the stability of MSeTe (M = Ti, Sn, and Ir) compounds, we calculated their cohesive and formation energies using the equations

$$\Delta E_c(\mathrm{MSeTe}) = E(\mathrm{MSeTe}) - E(M) - E(\mathrm{Se}) - E(\mathrm{Te}) \tag{1}$$

$$\Delta E_f(\mathrm{MSeTe}) = E(\mathrm{MSeTe}) - \frac{1}{2}E(\mathrm{MSe_2}) - \frac{1}{2}E(\mathrm{MTe_2}) \tag{2}$$

The resulting cohesive and formation energies are summarized in **Table 3**. The negative values observed for both sets of energies indicate the structural stability of these compounds, suggesting that they are energetically favorable and likely to be synthesized under appropriate conditions.

3.2. Elastic Properties

Elastic constants, denoted as “C_{ij},” serve as crucial indicators of a solid’s resilience against deformation and its reaction to external stresses. These constants are integral to the field of engineering, where they inform the selection of materials for optimized performance, ensuring both efficiency and safety in design. The quantity of independent elastic constants a material possesses is determined by the symmetry of its crystal structure. Specifically, hexagonal structures are characterized by five independent elastic constants: C_{11}, C_{12}, C_{13}, C_{33}, C_{44}.

Table 2. The calculated lattice parameters, ratio of lattice constants "*c/a*," and bulk modulus of MXY (M = Ti, Sn, Ir, X = Se, Te, Y = Se, Te) compounds in hexagonal close-packed CdI_2 structure and in the presence of the relativistic spin–orbit interaction within GGA exchange-correlation potential are compared. The experimental and theoretical values are taken from refs. [9,23,48,50,51,55,56,60,61] and [10,34,49,52–54,57–59] respectively.

		a = b (Å)	c (Å)	c/a	Bulk modulus [GPa]
$TiTe_2$	This work	3.599	6.022	1.67	78.6
	Other results	3.77,[34] 3.774[50] 3.777,[48,52] 3.767,[50] 3.78,[51] 3.779[34]	6.49,[34] 6.496[48] 6.539,[49] 6.498[48,50] 6.65,[51] 6.008[52] 6.817[34]	1.720[48] 1.732[49] 1.72[34]	
$TiSe_2$	This work	3.3727	5.8013	1.72	79.32
	Other results	3.540,[48] 3.774[49] 3.540,[52] 3.80[53]	6.008,[48] 5.995[49] 5.6953.[52] 5.90[53]	1.698[48] 1.732[49]	74.7[57]
TiSeTe	This work	3.6265	6.1531	1.69	75.03
	Other results	3.651[48]	6.317[48]	1.730[48]	
$SnTe_2$	This work	4.082	6.531	1.63	50.60
	Other results	4.11,[48] 4.10[49] 4.12[58]			
$SnSe_2$	This work	3.6926	6.5843	1.78	52.44
	Other results	3.63,[53] 3.811[55] 3.799,[54] 3.815[56] 3.84[58]	5.71,[53] 6.137[55] 5.908,[56] 6.144[58]		45.82[54]
SnSeTe	This work	4.0038	6.7665	1.69	46.59
	Other results	3.97[57]			
$IrTe_2$	This work	3.9674	5.3925	1.36	99.66
	Other results	3.930,[10] 3.928,[59,60] 3.930 ± 0.003 3.9284,[61] 3.9322,[9] 3.928[23]	5.386,[10] 5.405,[59,60] 5.393 ± 0.005 5.4049,[61] 5.3970[9] 5.405[23]	1.38[60] 1.38[61]	
IrSeTe	This work	3.8584	5.6461	1.46	101.82
$IrSe_2$	This work	3.8034	5.3746	1.41	103.26

We have determined the elastic constants for MSeTe (M = Ti, Sn, and Ir) compounds within GGA approach in nonmagnetic self-consistent calculations and hexagonal close-packed CdI_2 structure with spin–orbit interaction, with the results presented in **Table 4**. Due to the scarcity of experimental and theoretical data on these specific compounds—with the exception of $SnSe_2$ and $TiSe_2$—our comparisons are limited to these two compounds against available data.[54,62] The mechanical stability of these compounds is assessed through Born's stability criteria[63] for hexagonal crystals, which are as follows.

$$\begin{cases} C_{11} > |C_{12}|; \quad 2C_{13}^2 < C_{33}(C_{11} + C_{12}) \\ C_{44} > 0; \quad C_{66} > 0 \end{cases} \tag{3}$$

Table 3. The formation energy and cohesive energies of MSeTe (M = Ti, Sn and Ir) compounds within GGA approach in nonmagnetic self-consistent calculations and hexagonal close-packed CdI_2 structure with spin–orbit interaction.

Compounds	Formation energy (Ry)	Cohesive energy (Ry)
TiSeTe	−0.0874	−2.543
SnSeTe	−0.1284	−3.286
IrSeTe	−0.0048	−4.015

Our calculations affirm that all evaluated elastic constants adhere to these stability criteria, thereby confirming the mechanical stability of the compounds in question.

A notable observation from our analysis is that the $C_{11}(C_{22})$ component, indicative of atomic bonding strength along the *x*-direction (*y*-direction), is generally larger than other components especially C_{33}, suggesting that these compounds exhibit weaker bonding along the *z*-axis compared to the *x*- and *y*-axes. This also implies that the lattice constant in the z-direction (c) is more susceptible to changes induced by hydrostatic pressure and temperature compared to the lattice constants in the *x*- and *y*-directions (a and b). Most of the studied compounds, with the exception of $IrSe_2$, exhibit this characteristic. Particularly, the C_{33} value for the $SnSe_2$ compound is significantly less than the other components, highlighting the increased sensitivity of the c lattice constant to hydrostatic pressure and temperature in comparison to a and b.

Furthermore, we evaluated other mechanical properties such as bulk modulus (B_V, B_R and B_{Average}), Young's modulus (E_V, E and E_{Average}), shear modulus (G_V, G_R and G_{Average}), Poisson's ratio (ν_V, ν_R and ν_{Average}), Pugh's ratio (B/G), and the universal anisotropy index (A^U) to assess hardness, ductility or brittleness, and anisotropy in material behavior. These parameters for hexagonal crystal structure were derived from the elastic constants within Voigt's, Reuss's and Voigt–Reuss–Hill

Table 4. Computed elastic constants of MXY (M = Ti, Sn, Ir, X = Se, Te, Y = Se, Te) compounds within GGA approach in nonmagnetic self-consistent calculations and hexagonal close-packed CdI_2 structure with spin–orbit interaction.

Compounds		C_{11}	C_{12}	C_{13}	C_{33}	$C_{44} = C_{55}$	$C_{66} = (C_{11}-C_{12})/2$
$SnSe_2$	This work	103.28	35.23	32.25	33.42	36.28	34.02
	Theoretical results[54]	111.00	33.39	33.08	22.63	44.48	38.80
$SnTe_2$		126.65	45.24	54.44	55.37	63.20	40.71
$TiSe_2$	This work	128.65	40.24	51.44	52.38	60.28	44.21
	Experimental results[62]	120 ± 10	42 ± 10	–	39 ± 3	–	–
$TiTe_2$		108.26	40.24	64.80	97.95	65.25	34.01
$IrSe_2$		182.17	89.21	69.79	82.18	62.91	46.48
$IrTe_2$		173.85	69.16	58.04	59.19	58.34	52.35
SnSeTe		73.26	38.13	35.18	62.19	25.64	17.57
TiSeTe		113.27	46.28	56.15	76.05	63.54	33.49
IrSeTe		178.68	83.96	68.86	68.15	61.25	47.36

($\mathrm{VRH} = \frac{\mathrm{V+R}}{2}$) average approximations[64,65] using the following equations.

$$B_V = \frac{1}{9}[2(C_{11} + C_{12}) + C_{33} + 4C_{13}] \tag{4}$$

$$B_{\mathrm{R}} = \frac{C^2}{M} \tag{5}$$

$$G_{\mathrm{V}} = \frac{1}{30}[M + 12C_{44} + 12C_{66}] \tag{6}$$

$$G_{\mathrm{R}} = \frac{2}{5}\frac{[C^2 C_{44} C_{66}]}{[3B_V C_{44} C_{66} + C^2(C_{44} + C_{66})]} \tag{7}$$

where M and C^2 are calculated as follows.

$$M = C_{11} + C_{12} + 2C_{33} - 4C_{13} \tag{8}$$

$$C^2 = (C_{11} + C_{12})C_{33} - 2{C_{13}}^2 \tag{9}$$

In addition to, Young's modulus (E_{V}, E_R, and E_{VRH}) and Poisson's ratio (ν_{V}, ν_{R} and ν_{VRH}) within Voigt, Reuss, and Voigt–Reuss–Hill average approximations can be calculated using the calculated bulk modulus and shear modulus as follows.

$$E = \frac{9BG}{3B + G} \tag{10}$$

$$\upsilon = \frac{3B - 2G}{6B + 2G} \tag{11}$$

The calculated results of these compounds within GGA approach in nonmagnetic self-consistent calculations and in hexagonal close-packed CdI_2 with spin–orbit interaction are given in **Table 5**.

Among the compounds studied, SnSeTe exhibits the largest lattice constants, which correlates with it having the lowest bulk modulus. This suggests that SnSeTe is the most compressible compound within this group. Conversely, the $IrSe_2$ compound demonstrates the highest bulk modulus, indicating it is the least compressible.

The average bulk modulus of these compounds, except for SnSeTe and $SnSe_2$, aligns closely with the ranges observed in cast iron (58–107 GPa) and aluminum alloys (68–70 GPa).[66] Notably, the average bulk modulus of the $SnSe_2$ compound is comparable to that of magnesium alloys, which is ≈33.1 GPa.[66]

Shear modulus is a measure of a material's resistance to deformation under shear stress, while Young's modulus quantifies the relationship between stress and strain, reflecting a solid's stiffness and susceptibility to shape deformation from external forces. These moduli are pivotal in mechanical engineering for designing materials that meet specific stiffness requirements. Generally, a higher Young's modulus suggests that material is more challenging to stretch or deform, signifying a higher degree of stiffness. Similarly, a substantial shear modulus implies a higher rigidity

Comparative analysis of Young's and shear moduli across these compounds reveals that $IrSe_2$, with an average Young's modulus of 115.43 GPa, aligns with the typical ranges observed for Brass (102–125 GPa) and Bronze (96–120 GPa),[66] exhibiting the highest stiffness among the studied materials. This indicates a potentially enhanced level of covalent bonding in $IrSe_2$ compared to other compounds. However, while a higher Young's modulus generally suggests stronger bonding, it should not be viewed as the sole indicator of bond strength. The pronounced stiffness in IrSe2 may suggest a greater degree of covalent bonding, aligning with its mechanical properties, but these interpretations must consider a variety of influencing factors.

Conversely, $SnSe_2$ and SnSeTe display the lowest average Young's moduli, ranging from 50 to 90 GPa, akin to that of glass,[66] suggesting relatively weaker covalent bonds. In terms of shear modulus, $IrSe_2$ and SnSeTe demonstrate the highest and lowest values, respectively. $IrSe_2$'s shear modulus approximates that of Bronze at about 44.85 GPa, while SnSeTe's is closer to Cadmium's 18.97 GPa.[66] These findings offer deeper insights into the mechanical behavior and structural integrity of these compounds under various loading conditions.

Poisson's ratio (ν) and Pugh's ratio (B/G) are critical metrics for distinguishing between the ductility and brittleness of materials. Typically, a Poisson's ratio greater than 0.26 and a Pugh's ratio exceeding 1.75 indicates ductility, whereas values below

Table 5. Calculated bulk modulus (B), young's modulus (E), shear modulus (G), Poisson's ratio (ν), Pugh's ratio (B/G), and universal anisotropy index (A^U) of MXY (M = Ti, Sn, Ir, X = Se, Te, Y = Se, Te) compounds using the calculated elastic constants.

Compounds		SnSe$_2$	SnTe$_2$	TiTe$_2$	TiSe$_2$	TiSeTe	SnSeTe	IrTe$_2$	IrSe$_2$	IrSeTe
Bulk modulus (GPa)	B_V	48.83 45.82[54]	68.54	72.68	66.21	68.86	47.29	86.37	100.45	96.54
	B_R	33.38 31.26[54]	55.34	72.15	52.35	66.95	46.84	59.17	80.21	68.14
	$B_{Average}$	41.11 38.54[54]	61.94	72.42	59.28	67.91	47.06	72.77	90.34	82.34
Shear modulus (GPa)	G_V	30.66 37.32[54]	44.13	42.54	44.05	41.71	20.45	48.58	48.97	47.56
	G_R	21.85 29.45[54]	25.66	31.17	26.29	30.84	19.56	35.64	40.71	34.79
	$G_{Average}$	26.26 33.39[54]	34.89	36.86	35.17	36.28	20.01	42.11	44.84	41.18
Young's modulus (GPa)	E_V	76.07	108.99	106.79	108.18	104.12	53.62	122.73	126.38	122.56
	E_R	53.81	66.68	81.74	67.56	80.22	51.52	89.05	104.46	89.19
	$E_{Average}$	64.94 77.72[54]	88.13	94.53	88.09	92.39	52.57	105.91	115.43	105.87
Poisson's ratio (ν)	ν_V	0.240	0.235	0.255	0.228	0.248	0.311	0.263	0.290	0.288
	ν_R	0.231	0.299	0.311	0.284	0.300	0.316	0.249	0.283	0.281
	$\nu_{Average}$ e	0.230 0.16[54]	0.263	0.282	0.252	0.273	0.314	0.257	0.287	0.285
Pugh's ratio (B/G)	$(B/G)_V$	1.59	1.553	1.71	1.50	1.65	2.31	1.78	2.05	2.02
	$(B/G)_R$	1.53	2.156	2.31	1.99	2.17	2.39	1.66	1.97	1.96
	$(B/G)_{Average}$	1.56 1.15[54]	1.775	1.96	1.68	1.87	2.35	1.73	2.01	1.99
Anisotropy index (A^U)		2.84	3.84	1.83	3.64	1.78	0.23	2.27	1.26	2.25

these thresholds suggest brittleness.[67] In this study, the SnSe$_2$ compound is identified as more brittle compared to other materials. Conversely, SnSeTe is highlighted as the most ductile among the evaluated compounds, evidenced by its Poisson's ratio of 0.31.

For comparative purposes, we consider several other materials: ductile iron and cast iron, which both have Poisson's ratios ranging from 0.26 to 0.31 and 0.26 to 0.30, respectively, categorizing them within the ductile range. Copper, with a Poisson's ratio of ≈0.34, also demonstrates good ductility. In contrast, glass, with a Poisson's ratio approaching 0.20, is typically considered brittle, and silicon carbide (SiC), with a Poisson's ratio of about 0.14, is clearly indicative of brittleness.

The average Poisson's ratio for the compounds in this study, with the exception of SnSe$_2$, TiSe$_2$, and IrTe$_2$, falls almost within the range observed for both ductile and cast iron (0.26–0.31), suggesting a general trend towards ductility in these materials. This comparison helps to contextualize the mechanical behavior of the compounds relative to well-known industrial materials.

The mechanical properties of materials with elastic anisotropy vary depending on the direction of the applied external force. Thus, understanding a material's elastic anisotropy is crucial for predicting its response to different stress orientations. The universal anisotropy index (A^U) provides a measure of this property, calculated for solids of any symmetry as.

$$A^U = 5\frac{G_V}{G_R} + \frac{B_V}{B_R} - 6 \geq 0 \tag{12}$$

where B_V and G_V (and B_R and G_R, respectively) represent the bulk and shear moduli derived using Voigt's and Reuss's approximations.[64,65] A zero A^U value indicates isotropy in a solid, meaning its elastic response does not depend on the direction of force application. Conversely, a nonzero A^U value indicates anisotropic elasticity, where the mechanical properties are direction-dependent. Thus, A^U quantifies the degree of elastic anisotropy in solids.

Our calculations of A^U for the MSeTe (M = Ti, Sn, and Ir) compounds, as presented in Table 5, reveal that SnTe$_2$ possesses the highest A^U value, indicating significant elastic anisotropy and a mechanical response that is sensitive to the direction of external stress. On the other hand, SnSeTe compound exhibits the lowest A^U values, approaching almost zero, which suggests this material is nearly isotropic in its elasticity.

Constructing 3D surfaces of Young's moduli is an insightful method to visualize the elastic anisotropic properties of solids. In this approach, a perfectly spherical shape represents elastic isotropy in materials, where the mechanical properties are uniform in all directions. Any deviation from this spherical symmetry highlights the presence of elastic anisotropy, with the degree of deviation directly correlating to the extent of anisotropy.

A more pronounced departure from spherical symmetry signifies a higher level of elastic anisotropy.

Utilizing the ELATOOLS package, we computed the Young's moduli 3D surface constructions for the studied compounds, with the resulting visualizations displayed in **Figure 2**. Among these, the $SnTe_2$ compound exhibits the most significant deviation from spherical symmetry, indicating a pronounced elastic anisotropy. Conversely, SnSeTe compound shows minimal deviation, suggesting that this material possesses nearly isotropic elastic properties.

These visual and analytical results align with those derived from the universal anisotropy index (A^U), corroborating the observed elastic behaviors.

3.3. Electronic Properties

To explore the electronic properties of MXY (M = Ti, Sn, Ir, X = Se, Te, Y = Se, Te) compounds, calculations of their electron density of states (DOS) and band structures within the GGA approach in hexagonal close-packed CdI_2 with spin–orbit

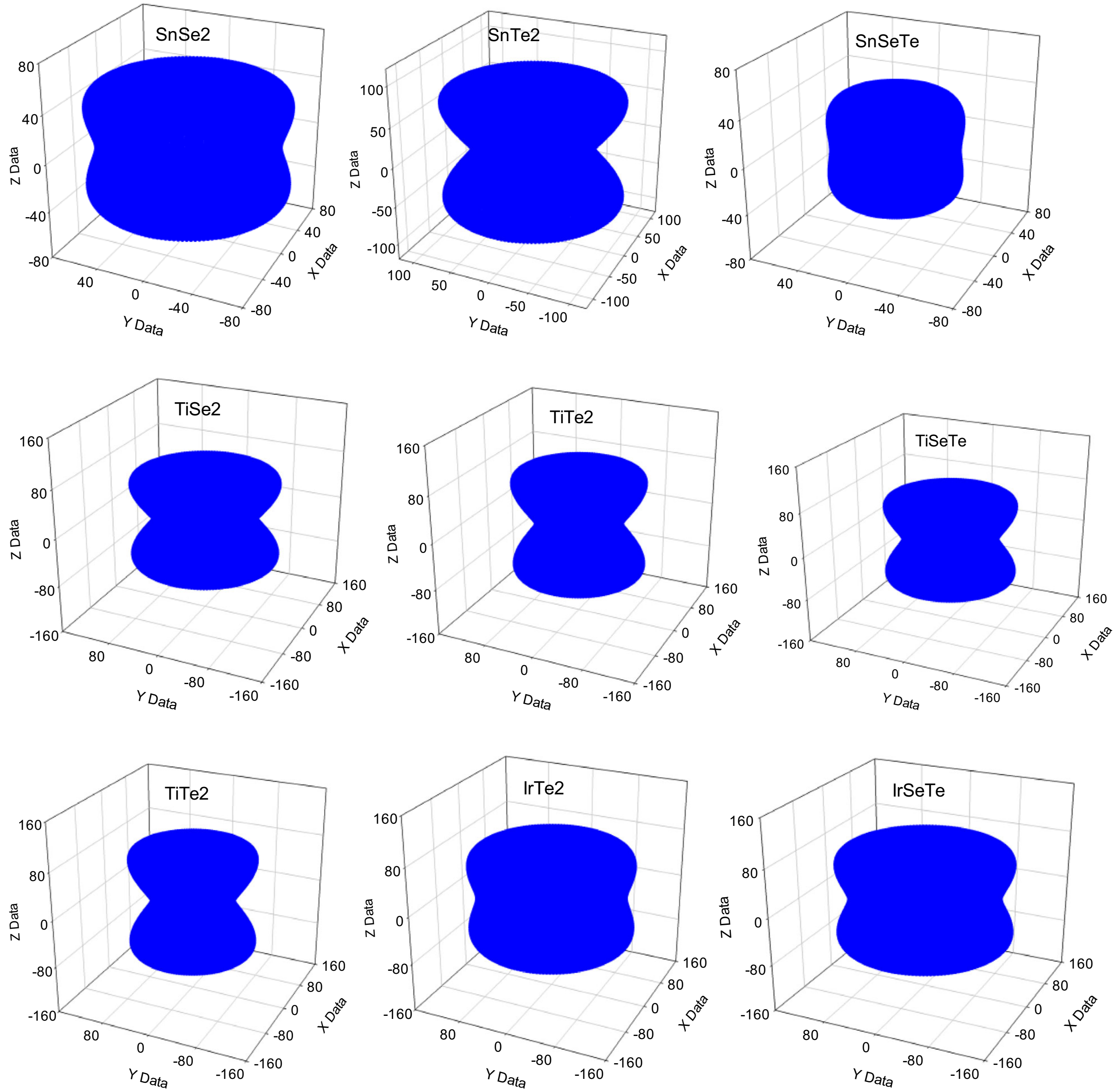
SnSe2
SnTe2
SnSeTe
TiSe2
TiTe2
TiSeTe
TiTe2
IrTe2
IrSeTe

Figure 2. 3D surface constructions of the Young's moduli of MXY (M = Ti, Sn, Ir, X = Se, Te, Y = Se, Te) compounds within the GGA approach in nonmagnetic self-consistent calculations and hexagonal close-packed CdI_2 crystal structure (space group $P\bar{3}m1$, No. 164) with spin–orbit interaction, depicted in GPa, showing the variations in elastic properties and anisotropy.

interaction were performed for comparative analysis. The electron DOS for these compounds, illustrated in **Figure 3**, indicates that except for SnSe2, all the compounds exhibit metallic characteristics, distinguished by their densities of states at the Fermi energy, $D(E_F)$.

Upon examining the DOS around the Fermi energy for Ti in both $TiSe_2$ and $TiTe_2$, similarities are observed in their behaviors. However, between -3 and -1 eV, differences emerge due to the varying hybridization of Ti's charge distribution with Te and Se atoms. Comparing $SnTe_2$ and $SnSe_2$, it's clear that $SnSe_2$ acts as an insulator with a small energy bandgap, whereas $SnTe_2$ presents metallic properties. The dominant contribution at the Fermi energy in $SnTe_2$ is attributed to the Te atom, with a minor share from Sn, pointing to significant Te–Sn hybridization effects on the electronic characteristics.

For assessing the transport properties of these compounds, the linear electronic-specific heat (γ) was calculated using the equation.

$$\gamma = \frac{\pi^2}{3} K_B^2 D(E_F) \tag{13}$$

where K_B represents the Boltzmann constant, and $D(E_F)$ denotes the density of states at the Fermi energy. Calculations of γ, derived from the DOS at Fermi energy, are also compiled in Table 1 for comparison. These findings reveal that IrXY

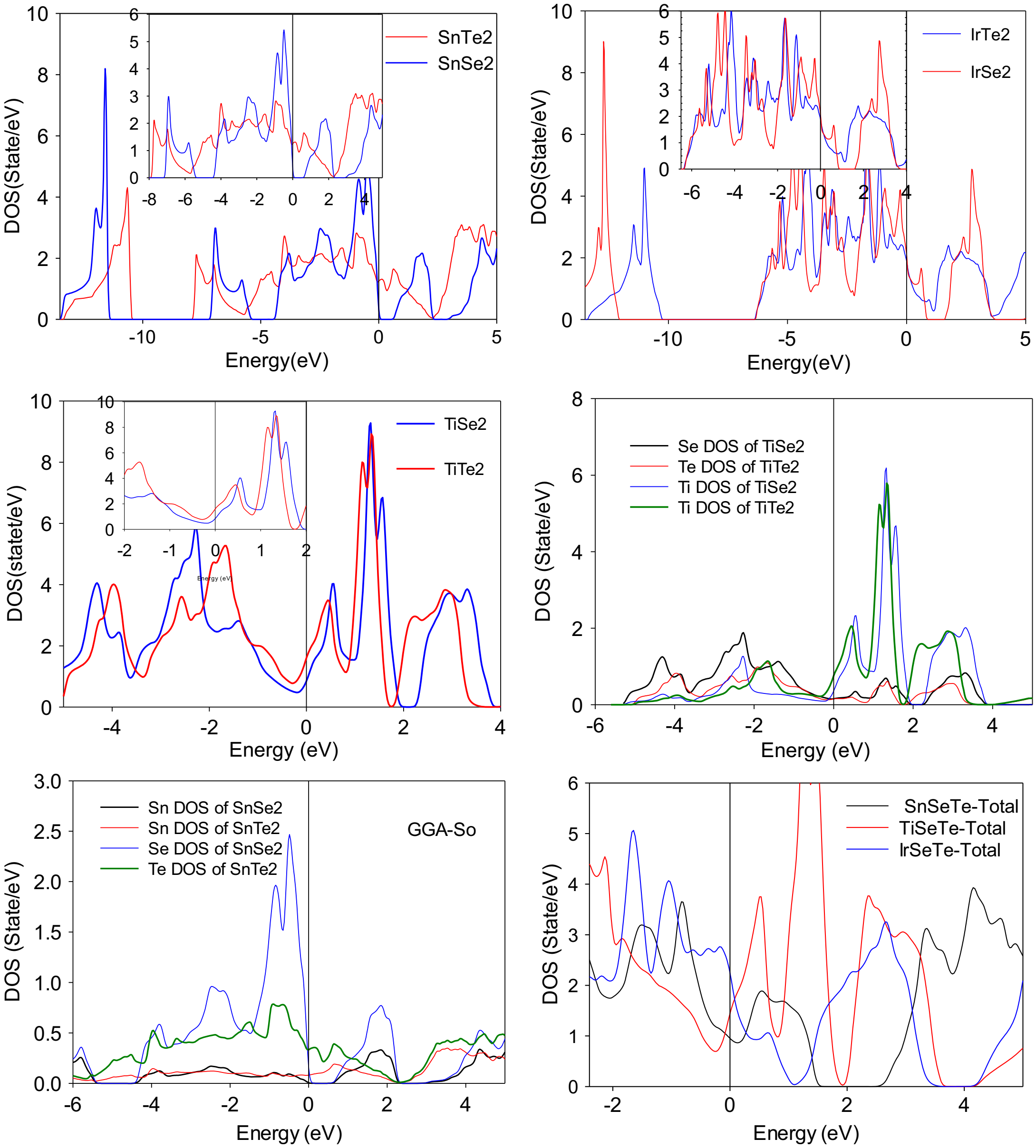

Figure 3. Comparison of the calculated total and partial electron densities of states for these compounds within the GGA approach in nonmagnetic self-consistent calculations and hexagonal close-packed CdI_2 crystal structure (space group $P\bar{3}m1$, No. 164) with spin–orbit interaction.

compounds have higher γ values than those of TiXY and SnXY, illustrating the influence of composition on electronic-specific heat. Notably, for MSe_2 compounds (M = Ir, Ti, and Sn), replacing a Se atom with a Te atom increases the γ value. Furthermore, the Sn atom's contribution to the linear electronic-specific heat in $SnTe_2$ is markedly lower than that of Te, emphasizing the impact of atomic interaction on transport properties.

To discern the impact of hydrostatic pressure on the electronic properties of MXY (M = Ti, Sn, Ir, X and Y = Se, Te) compounds, we computed the electron density of states (DOS) under

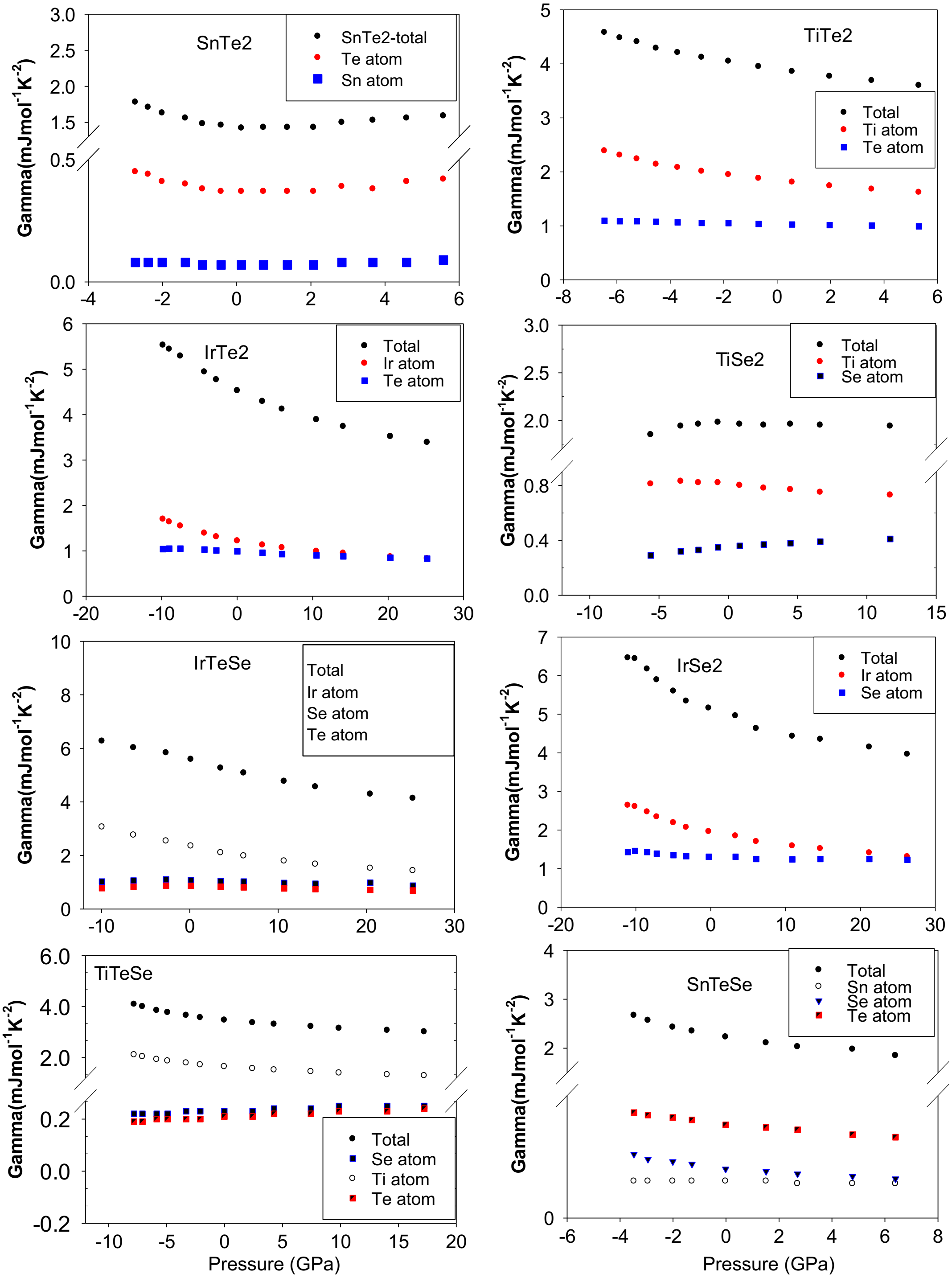

Figure 4. Variation of the linear electronic–specific heat for MXY compounds (excluding $SnSe_2$) under different hydrostatic pressures within the GGA approach in nonmagnetic self-consistent calculations and hexagonal close-packed CdI_2 crystal structure (space group $P\bar{3}m1$, No. 164) with spin–orbit interaction.

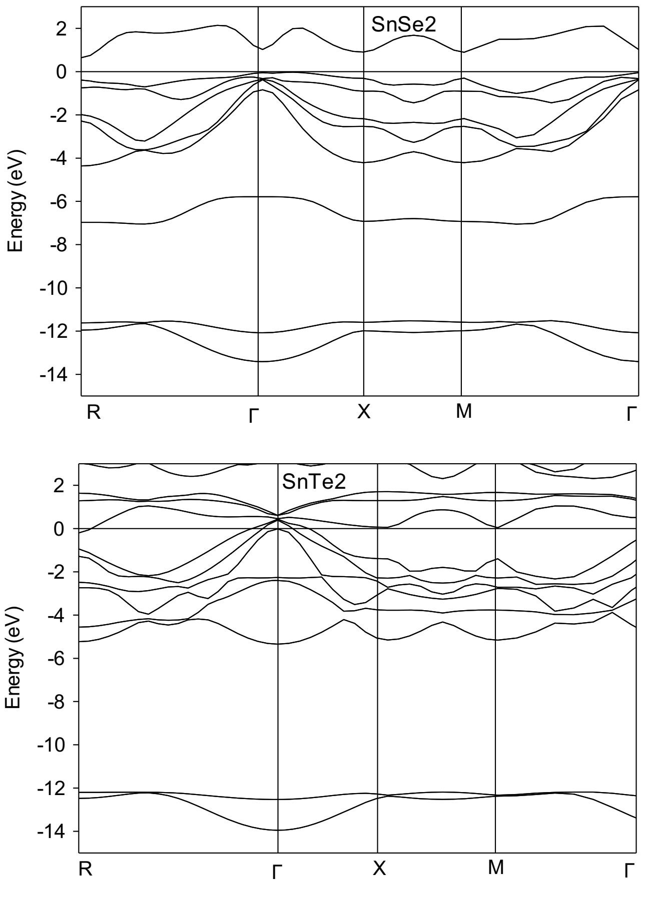

Figure 5. Band structures of $SnTe_2$, exhibiting metallic behavior, and $SnSe_2$, characterized by an indirect energy bandgap, as calculated within the GGA approach in nonmagnetic self-consistent calculations and hexagonal close-packed CdI_2 crystal structure (space group $P\bar{3}m1$, No. 164) with spin–orbit interaction.

varying pressures. The structural phase transition was not observed within the explored pressure range for these compounds. Except for $SnSe_2$, which displays semiconductor characteristics with a small indirect energy bandgap, all other compounds maintain metallic behavior across the assessed pressures.

Notably, there is a significant presence of electron charge at the Fermi energy for the MXY compounds (excluding $SnSe_2$). To further understand the influence of hydrostatic pressure on their transport properties, we calculated the linear electronic-specific heat (γ) at different pressures, based on the DOS at Fermi energy. The variation of γ with pressure is depicted in **Figure 4**. These findings highlight that Ti and Ir atoms contribute significantly to the linear electronic-specific heat of these compounds, whereas Te and Se atoms have a lesser impact.

Comparative analysis of the linear electronic specific heat (γ) across various pressures reveals distinct trends among the MXY compounds. Notably, the γ value for $IrTe_2$ is higher than that for $TiTe_2$ and decreases when the Ti atom is replaced by Sn in $SnTe_2$. Similarly, $TiSe_2$ exhibits a lower γ compared to $IrSe_2$, but this value increases when one Se atom is replaced by Te in IrTeSe. Additionally, substituting Ir with Ti and subsequently Ti with Sn in the IrTeSe compound leads to a decrease in γ.

Pressure generally reduces the linear electronic specific heat of these compounds. However, $SnTe_2$, $TiSe_2$, and TiTeSe show minimal impact from pressure changes, indicating specific compositional influences on their thermal properties under varying conditions.

Additionally, the band structures of these MXY compounds were calculated using various exchange-correlation potentials: GGA, Engel–Vosko, and mBJ. Given the similar behavior of the band structures across these potentials, only the band structures calculated in GGA with spin–orbit interaction are presented in **Figure 5**. We particularly focus on illustrating the band structures of two representative compounds: $SnTe_2$, exhibiting metallic behavior, and $SnSe_2$, featuring an energy bandgap.

The $TiSe_2$ compound is classified as a semimetal, characterized by a small overlap between the valence band maximum and the conduction band minimum. This overlap is indicative of negative band splitting, observed between Se–p electrons at the Γ point and Ti–d electrons around the Λ point. Notably, in this configuration, the conduction band is positioned at a higher energy level than the valence band. This negative splitting corroborates the findings of Traum et al.[68] and Chen et al.[69] $TiSe_2$ shows a semimetallic nature with a slight overlap of energy bands between the Γ and Λ symmetry points.

For $SnSe_2$, the valence band maximum and the conduction band minimum are located at the Γ and R points, respectively, indicating an indirect energy bandgap. The calculated indirect energy bandgaps of $SnSe_2$ within the GGA, Engel–Vosko, and mBJ potentials are compared with previously reported results[68,69] in **Table 6**.

This comprehensive analysis underscores the sensitivity of electronic and transport properties to external pressures and provides insight into the electronic structure variations among these compounds, further enriching our understanding of their potential applications in electronics and materials science.

The $SnSe_2$ compound, identified as a semiconductor with a small indirect energy bandgap across the pressures examined, shows varying responses to pressure changes in its electronic structure. To ascertain the pressure's impact on the energy

Table 6. The calculated indirect energy bandgap of $SnSe_2$ compound within GGA, Engel–Vosko, and mBJ approaches in hexagonal close-packed CdI_2 structure is compared with experimental and other theoretical results[69] within Heyd–Scuseria–Ernzerhof (HSE03 and HSE06) and GGA (PBE) functionals and other experimental result.[68]

GGA		Engel–Vosko		mBJ		Other experimental result[68]	Other theoretical results[69]
With SO	Without SO	With SO	Without SO	With SO	Without SO		
0.64	0.68	0.64	0.68	1.32	1.28	0.97	0.71 (PBE), 1.09 (HSE03), 1.48 (HSE06)

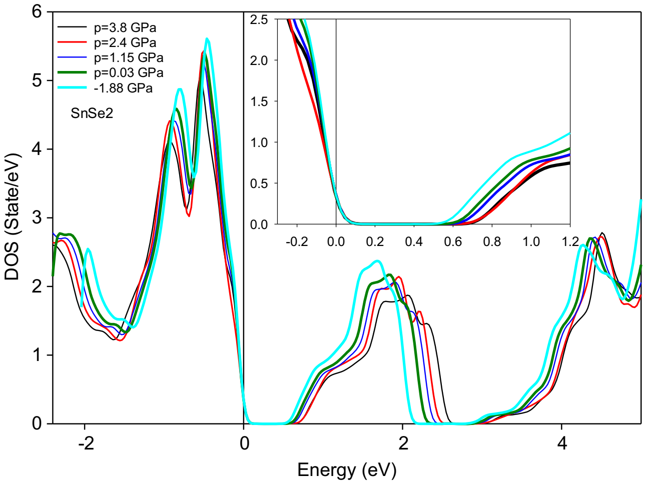

Figure 6. Electron density of states for the $SnSe_2$ compound across various pressures within the GGA approach in nonmagnetic self-consistent calculations and hexagonal close-packed CdI_2 crystal structure (space group $P\bar{3}m1$, No. 164) with spin–orbit interaction, illustrating pressure-induced shifts in electronic structure.

bandgap, we analyzed the electron density of states (DOS) within GGA approach at different pressures, as depicted in **Figure 6**. These analyses reveal that as pressure increases, the first DOS peak above the Fermi energy in $SnSe_2$ shifts towards higher energy levels, while the DOS below and near the Fermi energy remains largely unaffected. Consequently, the energy bandgap of $SnSe_2$ widens with an increase in pressure.

Given the bandgap's sensitivity to exchange and correlation energy, we calculated the bandgap of $SnSe_2$ under varying pressures and in the presence or absence of spin–orbit interaction, employing GGA, Engel–Vosko, and mBJ exchange-correlation potentials. The findings, illustrated in **Figure 7**, indicate that the bandgap widens from 0.5 eV at −3 GPa to 1.35 eV at 7.5 GPa across all applied potentials. To model this behavior quantitatively, we fitted the bandgap data using a quadratic polynomial

$$E_{\text{Gap}}(p) = E_{\text{Gap}}(0) + ap + bp^2 \tag{14}$$

where $E_{\text{Gap}}(p)$ represents the energy bandgap at pressure p, and $E_{\text{Gap}}(0)$ is the bandgap at zero pressure. The coefficients derived from this fitting, in the context of the presence and absence of spin–orbit interaction across the GGA, Engel–Vosko, and mBJ potentials, are presented in **Table 7**. The observed smaller magnitude of the b coefficient compared to a coefficient suggests that the pressure dependence of the bandgap tends towards a linear relationship.

This nonlinear behavior of energy bandgap of $SnSe_2$ and the linear electronic-specific heat of the other compounds to pressure can be attributed to variations in the degrees of ionic and covalent bonding under different pressures. These bonding variations, in turn, affect the Coulomb interactions due to changes in charge bonding behavior, highlighting the complex

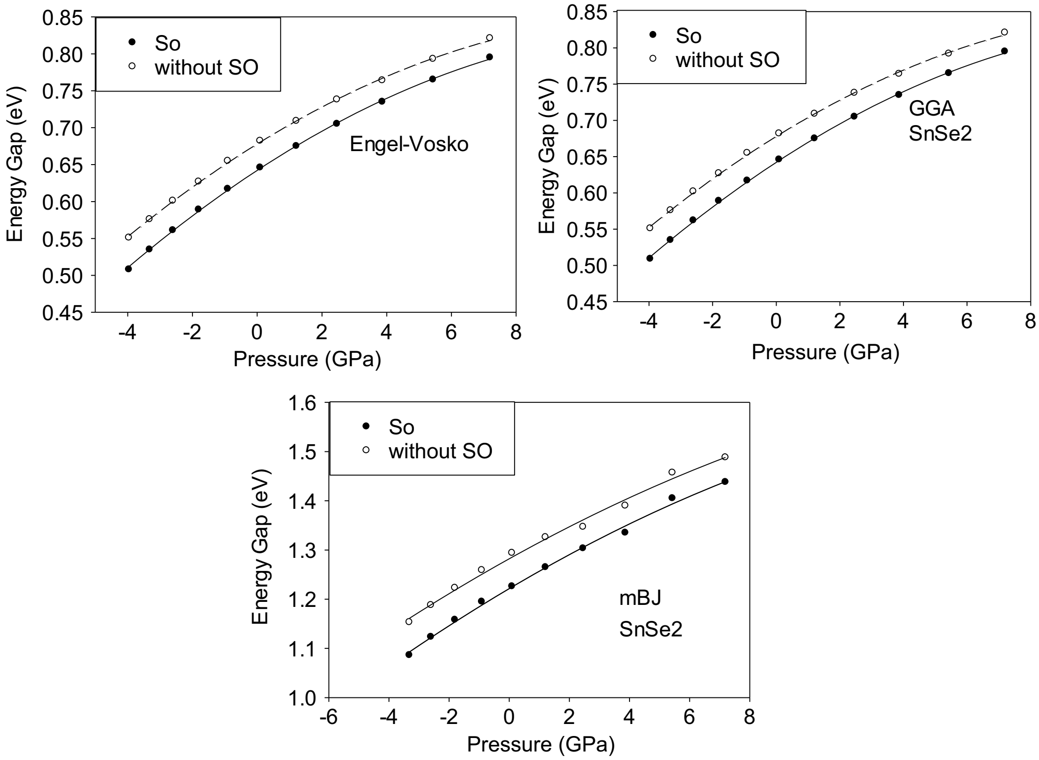

Figure 7. Energy bandgap variations of the $SnSe_2$ compound in nonmagnetic self-consistent calculations and hexagonal close-packed CdI_2 crystal structure (space group $P\bar{3}m1$, No. 164) with and without spin–orbit interaction, as determined within GGA, Engel–Vosko, and mBJ exchange-correlation potentials across a range of pressures.

Table 7. The calculated coefficients of this equation in the presence and absence of spin–orbit interaction within GGA, engle–vosko, and mBJ exchange and correlation potentials.

Exchange correlation energy	$E_{Gap}(0)$	$\times 10^{-2}$ a	$\times 10^{-3}$ b
GGA + SO	0.642	2.866	−1.074
GGA	0.678	2.713	−1.064
Engel–Vosko+SO	0.642	2.876	−1.088
Engel–Vosko	0.5587	2.718	−1.064
mBJ + SO	1.260	3.597	−1.633
mBJ	1.282	3.398	−0.747

interplay between pressure, electronic structure, and bonding characteristics in determining the electronic properties of these compounds.

To further explore the chemical bonding, the electron charge density distribution of XM_2 compounds was calculated using the GGA approach. The results, depicted in **Figure 8**, reveal predominantly circular electron charge density contours around the Ir, Sn, and Ti atoms, indicative of ionic bonding. This ionic character intensifies when replacing Ir with Sn, and further with Ti.

Electron charge transfer is observed between Se–Se, Se–Te, and Te–Te pairs. In $IrSe_2$, the maximum electron density primarily occurs along the Se–Se interactions, ranging between 0.5 and 0.7 e Å^{-3}. This density increases when one or both Se atoms are replaced with Te, resulting in values of 0.6–0.7 e Å^{-3} for $IrTe_2$ and 0.6–0.8 e Å^{-3} for IrSeTe. In contrast, $SnSe_2$ displays a significantly lower maximum electron density along Se–Se, between 0.1 and 0.3 e Å^{-3}, which increases with Te substitution to 0.6–0.9 e Å^{-3} for $SnTe_2$ and 0.5–0.9 e Å^{-3} for SnSeTe. $TiSe_2$ exhibits a higher baseline electron density along Se–Se, ranging from 0.4 to 0.9 e Å^{-3}, which remains relatively consistent with Te substitution, maintaining 0.5–0.9 e Å^{-3} for $SnTe_2$ and 0.6–0.9 e Å^{-3} for SnSeTe.

These findings indicate weak covalent Se–Se bonding in MSe_2 (M = Ir, Sn, Ti) compounds, attributable to shared electron density. A slight increase in covalent character upon Te substitution is noted, with the weakest covalent bonding observed in $SnSe_2$, highlighting subtle variations in bonding strength and electron distribution among these compounds.

3.4. Topological Band Order of XM_2 Compounds

The band structure is a crucial theoretical tool for determining the topological phase of materials. In this method, the topological phase is inferred from the topological band order.[1] Typically, forces such as spin–orbit interaction or external pressures can induce band splitting at high symmetry points near the Fermi energy. In topological metals or insulators, this band splitting can lead to a phenomenon known as topological band inversion,

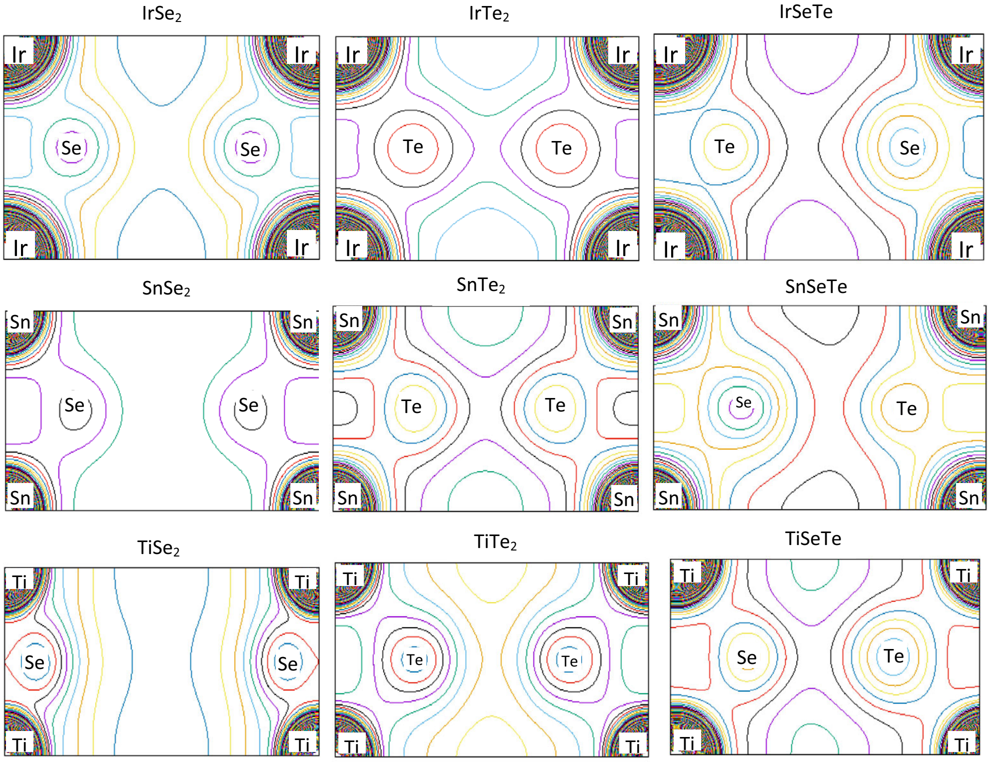

Figure 8. The electronic charge density contour of MXY (M = Ti, Sn, Ir, X = Se, Te, Y = Se, Te) compounds in the (001) crystallographic plane as calculated within the GGA approach in nonmagnetic self-consistent calculations and hexagonal close-packed CdI_2 crystal structure (space group $P\bar{3}m1$, No. 164) with spin–orbit interaction. Different colors show different electron density distributions and the contour interval of these electron density distributions is 0.1 e/Å^3.

where two orbitals with opposite parity swap positions within the band structure.

This inversion is critical for classifying materials as topological metals or insulators. Materials that exhibit band inversion, triggered by spin–orbit interactions and further influenced by external physical forces, meet the criteria for topological insulators or metals. This characteristic inversion underpins the unique electronic properties associated with topological phases, paving the way for novel quantum and electronic functionalities.

In investigating the topological phase of XM_2 (M = Ti, Sn, Ir; X = Se, Te,) compounds, particular attention was given to the distribution is very important of s, p, and d electrons within their band structures, both in the presence and absence of spin–orbit interaction, utilizing GGA, Engel–Vosko, and mBJ

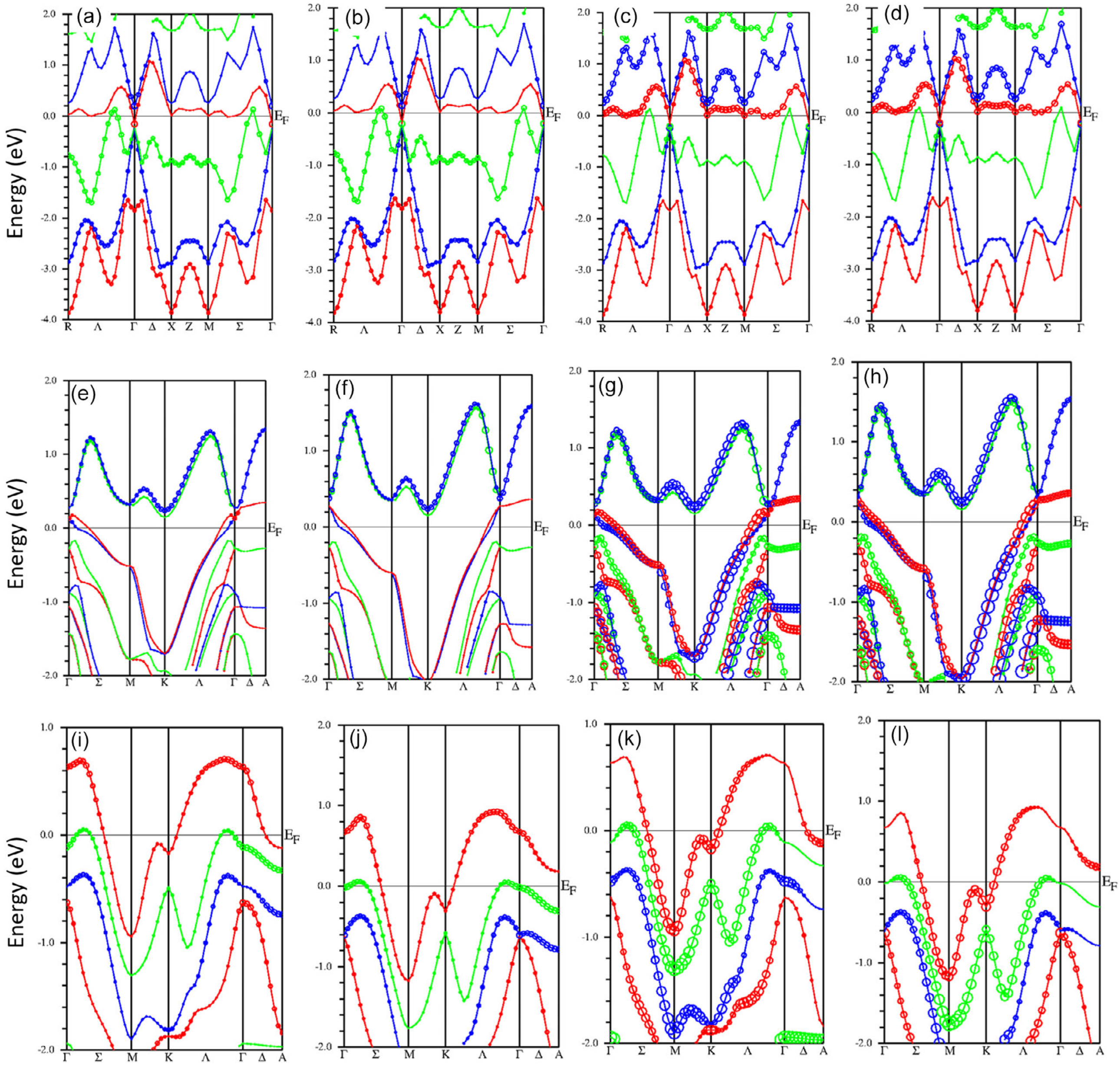

Figure 9. Orbital contributions to the band structures of $TiSe_2$, SnSeTe, and $IrSe_2$ within the GGA approach in nonmagnetic self-consistent calculations and hexagonal close-packed CdI_2 crystal structure (space group $P\bar{3}m1$, No. 164) at different pressures using distinct color-coded symbols to illustrate orbital types: a,c) p and d orbitals of $TiSe_2$ at zero pressure (red and green symbols respectively in (a) and (c)); b,d) p and d orbitals of $TiSe_2$ at 1.5 GPa (green and red symbols respectively in (b) and (d)); e,g) s and p orbitals of SnSeTe at zero pressure (red and blue symbols respectively in (e) and (g)); f,h) s and p orbitals of SnSeTe at 6.39 GPa (blue and red symbols respectively in (f) and (h)); i,k) p and d orbitals of IrSe2 at zero pressure (red and blue symbols respectively in (i) and (k)); j,l) p and d orbitals of IrSe2 at 26.3 GPa (blue and red symbols respectively in (j) and (l)). Each symbol's size is proportional to the degree of orbital contribution at each k-point, facilitating an understanding of the dynamic shifts in electronic structure under varying pressures.

exchange-correlation potentials. Initial calculations indicated that these compounds exhibit a normal band order at zero pressure, categorizing them as either normal metals or insulators under ambient conditions.

To assess the impact of hydrostatic pressure on the topological band order of these compounds, we meticulously analyzed the distribution of s, p, and d electrons in their band structures within GGA approach under varying pressures. Our findings indicate that most of the compounds retained a normal band order across all pressures tested, with no evidence of topological phase transitions. However, notable exceptions were observed in $TiSe_2$, $IrSe_2$, and SnSeTe, as illustrated in **Figure 9**.

Specifically, the predominant distribution of p and d electrons in $TiSe_2$ and $IrSe_2$ at the Γ symmetry point at zero pressure (indicated by red and green symbols for $TiSe_2$ in Figure 9a,c and red and blue symbols for $IrSe_2$ in Figure 9i,k) undergoes an inversion at pressures of 1.5 GPa and 26.3 GPa, respectively (shown by green and red symbols for $TiSe_2$ in Figure 9b,d, and blue and red symbols for $IrSe_2$ in Figure 9j,l). Similarly, the main distribution of s and p electrons in the SnSeTe compound at the Γ symmetry point at zero pressure (displayed with red and blue symbols in Figure 9e,g) is inverted at a pressure of 6.39 GPa (shown with blue and red symbols in Figure 9f,h).

This shift in electron distribution at the Γ point upon application of pressure indicates a band inversion between p and d orbitals for $TiSe_2$ and $IrSe_2$, and between s and p orbitals for SnSeTe. Consequently, the band structures of $TiSe_2$ and $IrSe_2$ exhibit a clear band inversion at the specified pressures, while SnSeTe shows a similar inversion at 6.4 GPa.

These phenomena suggest that $TiSe_2$, $IrSe_2$, and SnSeTe undergo topological phase transitions under pressure, corroborating previously reported findings for $TiSe_2$.[22] This confirmation enhances the credibility of our computational methods and offers profound insights into the pressure-induced topological phase transitions of these compounds. Such knowledge extends our understanding of their complex electronic behaviors and opens new avenues for exploring their potential applications in topological quantum devices.

Additionally, the electronic band structure of $TiSe_2$, as shown in Figure 9a, exhibits a minor overlap between the valence and conduction bands, indicative of its semimetal behavior, a characteristic discussed in Section 3.3.

4. Conclusion

This study presents an extensive analysis of the structural, elastic, electronic, and topological properties of MXY (M = Ti, Sn, Ir, X = Se, Te, Y = Se, Te) compounds through first-principles calculations that integrate spin-orbit interactions and hydrostatic pressure effects. Our findings demonstrate that these compounds predominantly exhibit stability in nonmagnetic phases, with significant alterations in their energy–volume curves driven by spin–orbit interactions, emphasizing its critical role in their material behavior.

The recalculated lattice parameters, ratio of lattice constants, and bulk moduli within the GGA exchange-correlation potential align well with existing experimental and theoretical data. Notably, the bulk modulus assessments reveal that IrXY compounds possess a greater resistance to compression than TiXY and SnXY compounds, indicative of stronger and potentially more covalent bonding characteristics.

Elastic constant analysis confirms mechanical stability across the studied compounds. $IrSe_2$ notably shows the highest stiffness, suggesting robust covalent bonding. This study also details the mechanical properties such as shear moduli, where $IrSe_2$ and SnSeTe show the highest and lowest values, respectively, indicating varied responses to shear stress across the series.

Electronic properties assessments reveal that while $SnSe_2$ behaves as a semiconductor with an indirect energy bandgap, all other studied compounds display metallic behavior characterized by diverse electron densities at the Fermi energy. The examination under varying pressures underscores the sensitivity of $SnSe_2$'s electronic properties to external pressure, with a notable increase in its energy bandgap.

From a topological perspective, detailed band structure analysis under different conditions shows that $TiSe_2$, $IrSe_2$, and SnSeTe undergo band inversions at specific pressures, signaling topological phase transitions. These transitions underscore the potential of these materials for applications in topological quantum devices.

In summary, this research enhances our understanding of the complex interplay between structure, bonding, and external influences in MXY (M = Ti, Sn, Ir, X = Se, Te, Y = Se, Te) compounds. The findings not only deepen insights into their inherent properties but also pave the way for exploiting these materials in advanced electronic and quantum applications. The integration of detailed electronic, structural, and topological analyses provides a solid foundation for further exploration and application of these fascinating materials.

Acknowledgements

DV acknowledges partial support from the National Science Foundation (NSF) under grant number CBET-2110603.

Conflict of Interest

The authors declare no conflict of interest.

Author Contributions

Munaf Aldaoseri: Data curation (equal); Formal analysis (equal); Investigation (equal); Validation (equal); Visualization (equal); Writing—original draft (equal). **Zahra Nourbakhsh**: Conceptualization (lead); Data curation (equal); Formal analysis (equal); Investigation (equal); Methodology (equal); Project administration (lead); Resources (lead); Software (lead); Supervision (equal); Validation (equal); Visualization (equal); Writing—original draft (equal). **Daryoosh Vashaee**: Conceptualization (equal); Formal analysis (equal); Funding acquisition (equal); Investigation (equal); Project administration (equal); Supervision (equal); Validation (equal); Writing—review and editing (equal).

Data Availability Statement

The data that support the findings of this study are available from the corresponding author upon reasonable request.

Keywords

density functional theories, energy bandgaps, linear electronic-specific heats, mechanical properties, topological phases

Received: June 23, 2024
Revised: September 2, 2024

[1] B. A. Bernevig, T. L. Hughes, S.-C. Zhang, *Science* **2006**, *314*, 1757.
[2] R. S. K. Mong, A. M. Essin, J. E. Moore, *Phys. Rev. B* **2010**, *81*, 245209.
[3] A. Hallouche, A. Hamri, S. Kacimi, A. Zaoui, *Phys. B* **2014**, *442*, 100.
[4] F. Kneidinger, E. Bauer, I. Zeiringer, P. Rogl, C. Blaas-Schenner, D. Reith, R. Podloucky, *Phys. C* **2015**, *514*, 388.
[5] D. Hsieh, D. Qian, L. Wray, Y. Xia, Y. S. Hor, R. J. Cava, M. Z. Hasan, *Nature* **2008**, *452*, 970.
[6] Y. Xia, D. Qian, D. Hsieh, L. Wray, A. Pal, H. Lin, A. Bansil, D. Grauer, Y. S. Hor, R. J. Cava, *Nat. Phys.* **2009**, *5*, 398.
[7] S. Jobic, P. Deniard, R. Brec, J. Rouxel, M. G. B. Drew, W. I. F. David, *J. Solid State Chem.* **1990**, *89*, 315.
[8] M. Shimakawa, K. Hayashi, *J. Alloys Compd.* **1997**, *259*, 219.
[9] A. F. Fang, G. Xu, T. Dong, P. Zheng, N. L. Wang, *Sci. Rep.* **2013**, *3*, 1153.
[10] S. Dey, V. K. Jain, *Platinum Metals Rev.* **2004**, *48*, 16.
[11] T. Zheng, C. Shang, Z. He, X. Wang, C. Cao, H. Li, P. R. Si, P. B. Pan, P. S. Zhou, P. J. Zeng, *Angew. Chem. Int. Ed.* **2019**, *131*, 14906.
[12] C. Sourisseau, R. Cavagnat, M. Fouassier, S. Jobic, P. Deniard, R. Brec, J. Rouxel, *J. Solid State Chem.* **1991**, *91*, 153.
[13] L. B. Barricelli, *Acta Cryst.* **1958**, *11*, 75.
[14] Y. Ding, B. Xiao, G. Tang, J. Hong, *J. Phys. Chem. C* **2017**, *121*, 225.
[15] B. L. Evans, R. A. Hazelwood, *J. Phys. D: Appl. Phys.* **1969**, *2*, 1507.
[16] J. Robertson, *J. Phys. C: Solid State Phys.* **1979**, *12*, 4753.
[17] K. M. Chung, D. Wamwangi, M. Woda, M. Wuttig, W. Bensch, *J. Appl. Phys.* **2008**, *103*, 083523.
[18] D. Abdel Hady, H. Soliman, A. El-Shazly, M. S. Mahmoud, *Vacuum* **1999**, *52*, 375.
[19] R. Bhatt, S. Bhattacharya, R. Basu, S. Ahmad, A. K. Chauhan, G. S. Okram, P. Bhatt, M. Roy, M. Navaneethan, Y. Hayakawa, A. K. Debnath, *ACS Appl. Mater. Interfaces* **2014**, *6*, 18619.
[20] Y. Gu, Y. Katsura, T. Yoshino, H. Takagi, K. Taniguchi, *Sci. Rep.* **2015**, *5*, 12486.
[21] Z. Zhu, Y. Cheng, U. Schwingenschlögl, *Sci. Rep.* **2014**, *4*, 4025.
[22] V. Rajaji, S. Janaky, S. C. Sarma, S. C. Peter, C. Narayana, *J. Phys. Condens. Matter* **2019**, *31*, 165401.
[23] J. M. Legera, A.S. Pereiraa, J. Hainesa, S. Jobicb, R. Brec, *J. Phys. Chem. Solids* **2000**, *61*, 27.
[24] T. Ritsche, Q. Stahl, M. Kusch, J. Trinckauf, G. Garbarino, V. Svitlyk, M. Mezouar, J. Yang, S.-W. Cheong, J. Geck, *Commun. Phys.* **2022**, *5*, 325.
[25] D. Ootsuki, H. Ishii, K. Kudo, M. Nohara, M. Arita, H. Namatame, M. Taniguchi, N. L. Saini, T. Mizokawa, *J. Phys. Chem. Solids* **2019**, *128*, 270.
[26] S. Koley, *Solid State Commun.* **2016**, *247*, 40.
[27] L. Zhang, X. Zhu, L. Ling, C. Zhang, L. Pi, Y. Zhang, *Philos. Mag.* **2014**, *94*, 439.
[28] K. Kim, S. Kim, K. T. Ko, H. Lee, J. H. Park, J. J. Yang, S. W. Cheong, B. I. Min, *Phys. Rev. Lett.* **2015**, *114*, 136401.
[29] K. Kim, S. Kim, B. I. Min, *Phys. Rev. B* **2014**, *90*, 195136.
[30] N. Lazarević, E. S. Bozin, M. Šćepanović, M. Opačić, H. Lei, C. Petrovic, Z. V. Popović, *Phys. Rev. B* **2014**, *89*, 224301.
[31] W.-H. Liu, J.-W. Luo, S.-S. Li, L.-W. Wang, *Phys. Rev. B* **2020**, *102*, 184308.
[32] M. Morsli, A. Bonnet, Y. Tregouet, A. Conan, S. Jobic, R. Brec, *Appl. Surf. Sci.* **1991**, *50*, 500.
[33] C. H. Liang, Y. H. Chan, K. K. Tiong, Y. S. Huang, D. O. Dumcenco, P. C. Liao, *J. Alloys Compd.* **2009**, *480*, 70.
[34] J. H. Gaby, B. Delong, F. C. Brown, R. Kirby, F. Lévy, *Solid State Commun.* **1981**, *39*, 1167.
[35] O. Anderson, G. Karschnick, R. Manzke, *Solid State Commun.* **1998**, *53*, 339.
[36] F. C. Brown, *Phys. B+C* **1980**, *99*, 264.
[37] K. Motizuki, Y. Yoshida, Y. Takaoka, *Phys. B+C* **1981**, *105*, 357.
[38] B. Guster, E. Canadell, M. Pruneda, P. Ordejón, *2D Mater.* **2018**, *5*, 025024.
[39] N. G. Stoffe, F. Levy, C. M. Bertoni, G. Margaritondo, *Solid State Commun.* **1982**, *41*, 53.
[40] W. Kohn, L. J. Shom, *Phys. Rev.* **1965**, *140*, A1133.
[41] K. Schwarz, P. Blaha, G. K. H. Madsen, *Comput. Phys.* **2002**, *147*, 71.
[42] P. Blaha, K. Schwarz, G. K. H. Madsen, D. Kvasnicka, J. Luitz, *wien2k: An Augmented Plane Wave+Local Orbitals Program for Calculating Crystal Properties*, Vienna University of Technology, Austria **2010**.
[43] J. P. Perdew, K. Burke, M. Ernzerhof, *Phys. Rev. Lett.* **1996**, *77*, 3865.
[44] E. Engel, S. H. Vosko, *Phys. Rev. B* **1994**, *50*, 10498.
[45] D. Koller, F. Tran, *Phys. Rev. B* **2012**, *85*, 155109.
[46] M. Jamal, M. Bilal, I. Ahmad, S. Jalali-Asadabadi, *J. Alloys Compd.* **2018**, *735*, 569.
[47] S. Yalameha, Z. Nourbakhsh, D. Vashaee, *Comput. Phys. Commun.* **2022**, *271*, 108195.
[48] Y. Arnaud, M. Chevreton, *J. Solid State Chem.* **1981**, *39*, 230.
[49] I. Oftedal, *Z. Phys. Chem* **1928**, *134*, 301.
[50] Y. Zhou, C. Chen, Y. Zhou, X. Chen, C. Gu, C. An, B. Zhang, Y. Yuan, H. Wu, R. Zhang, L. Zhang, X. Zhu, X. Yang, Z. Yang, *Phys. Rev. B* **2019**, *99*, 125104.
[51] M. Zhang, X. Wang, A. Rahman, Q. Zeng, D. Huang, R. Dai, Z. Wang, Z. Zhang, *Appl. Phys. Lett.* **2018**, *112*, 041907.
[52] N. V. Podberezskaya, S. A. Magarill, N. V. Pervukhina, S. V. Borisov, *J. Struct. Chem.* **2001**, *42*, 654.
[53] H. Wang, Y. Gao, G. Liu, *RSC Adv.* **2017**, *7*, 8098.
[54] X. He, H. Shen, *Phys. B* **2012**, *407*, 1146.
[55] C. Julien, M. Eddrief, I. Samaras, M. Balkanski, *Mater. Sci. Eng. B* **1992**, *15*, 70.
[56] V. G. Hadjiev, D. De, H. B. Peng, J. Manongdo, A. M. Guloy, *Phys. Rev. B* **2013**, *87*, 104302.
[57] M. M. Alyoruk, Y. Aierken, D. Cakir, F. M. Peeters, C. Sevik, *J. Phys. Chem. C* **2015**, *119*, 23231.
[58] E. M. Flores, V. J. R. Rivera, M. J. Piotrowski, E. J. S. Sacari, J. R. Sambrano, M. L. Moreira, **2023**, http://dx.doi.org/10.2139/ssrn.4635900.
[59] S. Jobic, R. Brec, J. Rouxel, *J. Alloys Compd.* **1992**, *178*, 253.
[60] E. F. Hockings, J. G. White, *J. Phys. Chem.* **1960**, *64*, 1042.
[61] S. Jobic, P. Deniard, R. Brec, J. Rouxel, A. Jouanneaux, A. N. Fitch, *Zeitschrift für anorganische und allgemeine Chemie* **1991**, *598*, 199.
[62] W. G. Stirling, B. Dorner, J. D. N. Cheeke, J. Revelli, *Solid State Commun.* **1976**, *18*, 931.
[63] M. Born, in *Math. Proc. Cambridge Philos. Soc.* **1940**, Vol. *36*, p. 160.
[64] W. Voigt, in *Lehrbuch der kristallphysik:(mit ausschluss der kristalloptik)*, Vol. *34*, BG. Teubner, Leipzig **1910**.
[65] A. Reuss, *J. Appl. Math. Mech.* **1929**, *9*, 49.
[66] https://www.engineeringtoolbox.com/young-modulus-d_417.html, accessed: May, 2024.
[67] D. G. Pettifor, *Mater. Sci. Technol.* **2013**, *8*, 345.
[68] M. M. Traum, G. Margaritondo, N. V. Smith, J. E. Rowe, F. J. Di Salvo, *Phys. Rev. B* **1978**, *17*, 1836.
[69] C. H. Chen, W. Fabian, F. C. Brown, K. C. Woo, B. Davies, B. DeLong, A. H. Thompson, *Phys. Rev. B* **1980**, *21*, 615.